ORIGINAL PAPER

An Experimental Investigation of the Effects of Grain Size and Pore Network on the Durability of Vicenza Stone

S. Scrivano[1] · L. Gaggero[1] · J. Gisbert Aguilar[2]

Abstract

The textural properties of a rock and the characteristics of its pore network are intrinsic variables to consider when investigating the resistance of rock to weathering. To establish the influence of these variables on the effectiveness and progression of weathering processes, two lithotypes of a limestone were analyzed with respect to their texture and porosity, and to their performance during artificial weathering experiments. The studied rock is Vicenza Stone, a bioclastic limestone with heterogeneous texture, variable grain size from fine to coarse, and high levels of open porosity (27–28%). Two sets of samples were obtained from a quarry, defining coarse-grained (CGV) and fine-grained (FGV) lithotypes of Vicenza Stone. Multiple techniques (optical microscopy, scanning electron microscopy, image analysis, mercury intrusion porosimetry, hygroscopicity, ultrasound, and water absorption) were used to characterize the texture and porosity of the limestone. The sample sets were subjected to freeze–thaw (UNI 11186:2008, Cultural heritage—Natural and artificial stone—Methodology for exposure to freeze-thawing cycles, 2008) and salt-crystallization (partial continuous immersion method with a Na_2SO_4-saturated saline solution) weathering experiments to investigate the processes and progression of mechanical and chemical weathering. Differences in freeze–thaw-induced micro-cracks and in the deposition of secondary micrite between the lithotypes show that the CGV has an overall higher susceptibility to freeze–thaw weathering than FGV. Salt-weathering processes induced micro-crack formation, material dissolution, and secondary precipitation, suggesting the simultaneous occurrence of mechanical stress and chemical dissolution–precipitation processes. FGV is more prone to salt-induced weathering than CGV, whereas CGV is susceptible to the wide thermal excursions of freeze–thaw weathering.

Keywords Vicenza stone · Grain size · Porosity · Weathering · Freeze–thaw · Salt weathering · Durability

1 Introduction

Calcareous sedimentary rocks are widely used as ornamental and dimension stones because of the ease of working and polishing of such rocks. However, the mineralogical compositions and petrophysical features of such materials usually confer them with rather low durability. The present work investigates the texture and porosity, and weathering progression/evolution of Vicenza Stone, a bioclastic limestone that is widely adopted in NE Italy for use in both indoor and outdoor environments. The sedimentary variability of this limestone means that different facies of the rock may show different durabilities with respect to weathering. The close correlation between porosity and the weathering susceptibility of rock exposed outdoors is well documented (Iñigo et al. 2000). It has been shown that the pore network is the primary site of exchange between the bulk of the rock and fluids in the atmosphere (e.g., air, water, and chemical solutions; Yu and Oguchi 2010; Ballesteros et al. 2011; Benavente 2011; Molina et al. 2011; Di Benedetto et al. 2015).

Pore openings can have a wide range of radii, which means that characterizing such spaces usually requires the application of multiple techniques to obtain information at various scales with adequate resolution. For example, the investigation of the hygroscopic properties of natural rock requires techniques with optimal resolutions of 0.001–0.100 μm. Similarly, to study capillary rise, the analysis should be focused on a size range of 0.1–1000.0 μm.

✉ S. Scrivano
  simona.scrivano@edu.unige.it

1 Department of Earth, Environment and Life Sciences, University of Genoa, Corso Europa 26, 16132 Genoa, Italy

2 Department of Earth Sciences, University of Zaragoza, Campus San Francisco, Pedro Cerbuna 12, 50009 Zaragoza, Spain

Given that the aim of this study is to evaluate the influence of petrophysical parameters on weathering processes, the investigation of the entire range of pore radii required the use of a multiple-technique approach. Although several studies have investigated the correlation of microstructural characteristics (mainly porosity) with weathering susceptibility, few have assessed the influence of effective surface area on weathering processes (Franzoni and Sassoni 2011). In the present work, grain size was investigated along with pore size distribution to establish their influence on durability via measurements of effective surface area.

2 Materials and Methods

2.1 Vicenza Stone

2.1.1 Geological Setting

"Vicenza Stone" refers to the Oligocene bioclastic limestone from the Berici Hills in the sub-Alpine area of NE Italy (Fig. 1a). The main structure of these hills is an eroded anticline bearing Upper Cretaceous to Miocene formations.

The Berici Hills are located at the southeastern end of the Alpine–Chiampo graben and host two different quarry zones. During the Oligocene, a carbonate platform developed under shallow-marine conditions and then transitioned to a deep-marine environment. A lagoon was linked to the open sea through channels across the reef. In this tropical paleo-environment white Castelgomberto calcarenite, including Vicenza Stone was deposited. Vicenza Stone corresponds to nullipore back-reef limestones formed in oxic tide channels during the lagoon phase, following the deposition of mud, sand, plant fragments, and shells (Bosellini and Trevisani 1992).

2.1.2 Petrographic and Mineralogical Features

Vicenza Stone is a bioclastic limestone in which variably fragmented bioclasts are commonly recrystallized and replaced by sparry calcite and cemented by a matrix of micrite, Fe-oxides, and hydroxides (Fig. 1b; Cornale and Rosanò 1994). The heterogeneous texture is characterized by variable fine to coarse grain size and high porosity (ca. 28% in volume). According to the Folk classification (Folk 1959, 1962), Vicenza Stone is a biomicrite, and the poorly sorted
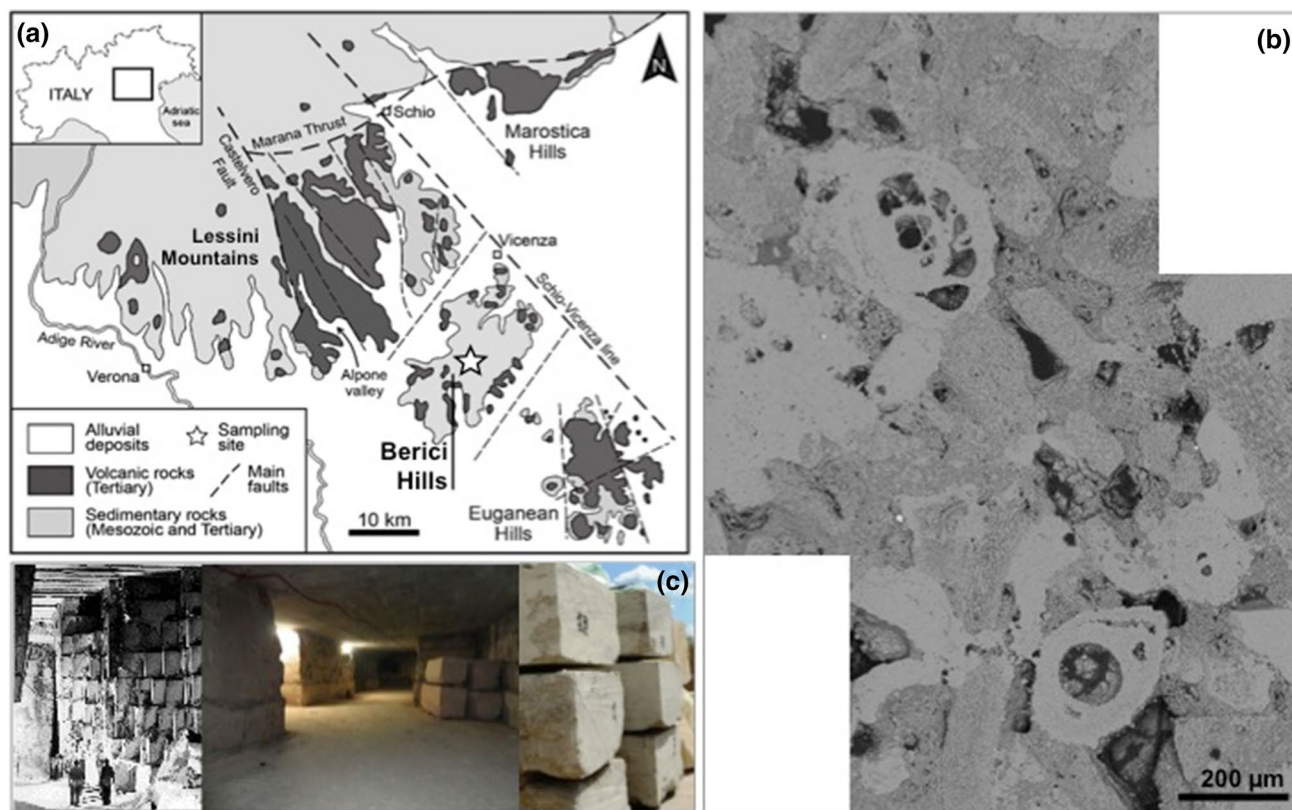

Fig. 1 Vicenza Stone. **a** Simplified geological map of the area surrounding Badia quarry in Zovencedo, northeastern Italy (modified after Mattioli et al. 2016). **b** SEM photomicrograph of the grain-supported fabric of the limestone. Bioclasts are the prevailing grains. **c** The Badia quarry, showing indoor pillars and chambers with piled blocks of Vicenza Stone outside

and clast-supported texture also defines it as grainstone (Dunham 1962). The majority of the bioclasts are nummulites, sponges, red algae, bryozoans, corals, and foraminifera. The rock comprises calcite ($CaCO_3$) ($> 99\%$ by volume) and rare Fe-oxides and hydroxides.

2.1.3 Samples

The samples were obtained from Badia quarry [locality: Zovencedo (Vicenza); Fig. 1c]. The extraction site has a high quarry front (> 10 m) in which fining-upward textures can be observed. This allowed the sample set to be defined and divided into two lithotypes according to grain size, namely coarse-grained (CGV) and fine-grained (FGV) Vicenza Stone (Fig. 2).

The petrophysical characterizations of the limestone (i.e., using capillary absorption, ultrasound, and total immersion) were conducted on six cubic specimens for each lithotype and for the different states of samples (unweathered, salt weathered, or freeze–thaw weathered). The image-based observations (i.e., optical microscopy; scanning electron microscopy, SEM; and digital image analysis, DIA) were performed on thin sections, polished chips, and small parallelepiped samples (1 cm × 1 cm × 2 cm). Overall, 18 cubic samples measuring 5 cm × 5 cm × 5 cm and 12 cubic samples measuring 3 cm × 3 cm × 3 cm samples were analyzed.

2.2 Analytical Techniques

2.2.1 Digital Image Analysis

Digital image analysis is a software-based method for analyzing microscope images to quantify selected parameters (e.g., pore diameter, grain size, and grain shape; Mueller and Hansen 2001). The analyses in the present study were conducted using high-resolution macro-photographs and SEM images obtained with a Tescan Vega 3 LM scanning electron microscope located at the Department of Earth, Environment and Life Sciences (DISTAV) of the University of Genoa, Italy. The macro-photographs of the samples, which were color-treated to highlight voids, were obtained with a Canon EOS Rebel T3 device and treated with photographic filters to obtain the best pictures for the subsequent image analysis. SEM images were obtained under high-vacuum conditions using an optimized ratio between back-scattered and secondary electrons to obtain the best signal and most complete information set. The ImageJ open-source software (Crawford and Mortensen 2009) was used to acquire the data for porosity and pore parameters (mainly shape and size) from each image. The analysis based on both macro-photographs and SEM images used the following steps: (1) the definition of the threshold of the gray-scale 8-bit images to obtain binary images, (2) the segmentation and automated recognition of
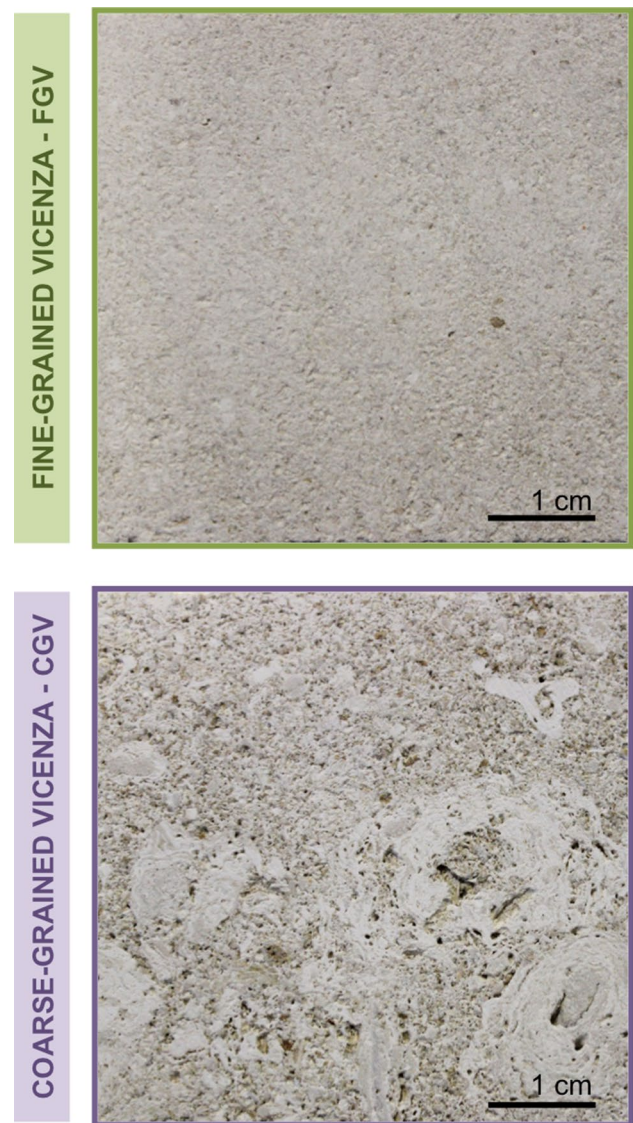

Fig. 2 Macro-photographs of the two lithotypes, FGV and CGV, showing the differences in texture and grain size

the pore space, and (3) the application of calculus routines to calculate selected pore size and shape parameters (pore area, pore perimeter, maximum and minimum axes, and circularity). The threshold identification process, which is crucial for the ensuing steps, is operator-dependent (pixel selection is delegate to the analysts) and, therefore, influences the measurement of pore area. JMicrovision software (Roduit 2007) was used to build the dataset for grain size and grain orientation for each image (Gioncada et al. 2011). This program was used to analyze SEM images, the results are obtained with an automated routine based on the recognition of grains by color shade, but can be controlled manually by selecting each grain to be counted and analyzed. Both software packages apply a relationship between pixels from the analyzed

images and physical dimensions (measured in microns) to calculate the geometrical parameters describing pore space.

2.2.2 Relative Mass Loss

The relative mass loss (ΔM) (%) was used as a measure of the degree of weathering induced during the artificial weathering experiments described in Sect. 2.3. This measure is recommended for evaluating physical deterioration according to UNI EN 12370:2001 and the present study involved recording the mass of the dried sample before salt weathering (m_0) and after salt weathering (m_d) and calculating by

$$\Delta M = \left(\left(m_0 - m_d \right) / m_d \right) \times 100. \tag{1}$$

The calculation was similarly applied to the freeze–thaw-weathered samples to estimate material loss during those experiments.

2.2.3 Mercury Intrusion Porosimetry (MIP)

The porosimetry measurements were performed with the Pascal 140 and Pascal 240 combined porosimeter instrumentation system at the Department of Civil, Chemical, and Environmental Engineering (DICCA) of the University of Genoa. This instrumental set-up ensures a wide measurement range at pressures ranging from ambient to 200 MPa. The apparatus operates in association with the software Solid®, which calculates various porosity-related parameters, including apparent and bulk density, pore volume (total and incremental), porosity, specific surface area, and average pore and particle sizes along with their distributions (Mayer–Stowe model).

Using the measured porosimetric data, two parameters were calculated to evaluate the durability of the limestone lithotype samples in terms of their susceptibility to freeze–thaw and saline-solution weathering. The first parameter was the Maage Durability Factor (F_c; Maage 1990), which relates pore size distribution to the susceptibility to freeze–thaw weathering as follows:

$$F_c = \left(3.2 / V_{\Phi t} \right) + \left(2.4 \times V_{\Phi > 3\mu m} \right), \tag{2}$$

where $V_{\Phi t}$ is the total pore volume in cm^3 and $V_{\Phi > 3\mu m}$ is the fraction of pore volume taken up by pores with radii of > 3 μm. Calculated F_c values of < 70 mean that the material is susceptible to freeze–thaw weathering, whereas values of ≥ 70 mean that the material is resistant to such weathering.

The second parameter calculated was the Salt Susceptibility Index (SSI; Yu and Oguchi 2010), which relates salt-induced weathering to pore size distribution as follows:

$$\text{SSI} = \left(I_{\Phi t} + I_{\Phi < 0.1\,\mu m} \right) \times \left(V_{\Phi < 5\,\mu m} / V_{\Phi t} \right), \tag{3}$$

where $I_{\Phi t}$ is the index of total connected porosity, $I_{\Phi < 0.1\mu m}$ is the index of the micro-porosity of pores smaller than 0.1 μm in radius, $V_{\Phi t}$ is the volume of total connected porosity, and $V_{\Phi < 5\mu m}$ is the volume of micropores smaller than 5 μm in radius. SSI values of < 4 mean that the material is resistant to salt-induced weathering, whereas values of ≥ 4 mean that the material is susceptible to such weathering. One unweathered sample and one salt-weathered sample were analyzed for each rock lithotype. The tested samples were fragments of about 1 g and were oven dried to constant weight prior to analysis.

2.2.4 Total Immersion

The test used to measure the volume of water absorbed by the samples during total immersion followed that specified in UNI EN 13755:2008 (2008). In the test, dried cubic specimens are immersed in deionized water and periodically removed to be weighed at predetermined time intervals (30, 60, 120, 240, 1080, 1320, 1560, 1920, and 2400 min) until a maximum mass is reached, or otherwise up to a period of 8 days (11,520 min). The mass data (with a precision of 0.01 g) are used to calculate values of absorbed water (Ab) as follows:

$$\text{Ab} = \left[\left(m_s - m_d \right) / m_d \right] \times 100, \tag{4}$$

where m_s is the mass of the saturated sample at each time point, and m_d is the mass of the dried sample. A relationship can then be established between Ab and time.

For the present study, the test was first run in the standard way as described above and then in a modified way using an automated measurement apparatus (Plattner et al. 2012) at the University of Zaragoza. The automated procedure involved the use of a balance to constantly monitor water absorption by measuring the mass of the specimen immersed in water at a 1-s interval for the entire duration of the absorption process. For the automated procedure, the experiment ended when the difference between two subsequent measurements of mass was less than 0.1% of the whole specimen mass. For the standard experiments the sample set comprised three 5 cm × 5 cm × 5 cm samples, for each lithotype and conservation state, while for the modified test the sample set comprised three 3 cm × 3 cm × 3 cm samples for each lithotype and conservation state (18 samples overall). The average data (recast between standard and modified experiments) were used to calculate Ab and the open pore volume.

2.2.5 Capillary Uptake

The test used to measure capillary uptake followed that specified in UNI EN 15801:2010 (2010). In the test, a dried cubic specimen is placed onto a saturated bedding layer

and weighed at given times (depending on the porosity of the lithotype) until the difference between two subsequent measures is less than 1% of the whole specimen mass. The mass data (with a precision of 0.01 g) are used to calculate values of absorbed water per unit area (Q_i) values at different elapsed times, as follows:

$$Q_i = [(m_i - m_d)/A], \tag{5}$$

where m_i is the mass of the sample at each time interval, m_d is the mass of the dried sample, and A is the area of the face in direct contact with the bedding layer. A relationship can then be established between Q_i and time.

For the present study, the capillary uptake test was first run in the standard way as described above and then in a modified way using an automated measurement apparatus developed at the University of Zaragoza. The equipment allowed water absorption by capillary uptake to be constantly monitored by measuring the mass of absorbed water at a 1-s interval for the entire duration of the process. For the standard experiments the sample set comprised three 5 cm × 5 cm × 5 cm samples, for each lithotype and conservation state, while for the modified test the sample set comprised three 3 cm × 3 cm × 3 cm samples for each lithotype and conservation state (overall 18 samples). The average data (recast between standard and modified experiments) were used to calculate values of Q_i for different elapsed times as well as values of the capillary water absorption coefficient (AC; the slope of the linear section of the curve obtained by plotting Q_i versus the square root of time).

2.2.6 Ultrasound Velocity

Ultrasound velocity was obtained by directly measuring (Kahraman 2007) the elastic longitudinal wave velocity (V_p) with a C-730 ultrasonic tester at the University of Zaragoza. Three samples measuring 5 cm × 5 cm × 5 cm were analyzed for each lithotype, with nine measurements being made for a single test and the mean taken as a representative value. The samples were oven dried at a constant temperature of 60 °C for 48 h to achieve constant mass. The end surfaces of the samples were polished to provide high-quality coupling with the transducers to obtain accurate measurements.

2.3 Artificial Weathering Experiments

2.3.1 Freeze–Thaw Weathering

The procedure for the freeze–thaw-weathering experiments followed that specified in UNI 11186:2008. In the experiments, saturated cubic specimens were subjected to a succession of 32 freeze–thaw cycles of 8 h each. Each 8-h cycle constituted 2 h of cooling from 20 °C to −20 °C, followed by 2 h at −20 °C, followed by 2 h of warming in water from

−20 °C to 20 °C, followed by 2 h at 20 °C. The testing was carried out at the laboratories of the Department of Civil, Chemical and Environmental Engineering DICCA of the University of Genoa using automated apparatus. Six cubic samples of each rock type were tested over 16 cycles of treatment, and another six samples were tested over 32 cycles (Fig. 3). These two experiment durations allowed the evolution of the weathering processes to be better determined.

2.3.2 Salt Weathering

The continuous partial-immersion procedure used in the present study to measure salt weathering followed that specified by Benavente et al. (2001). The procedure is characterized by a continuous fueling of the system, as the samples are always immersed to 10% of their height in a saturated saline solution. The experiment progresses for 15 cycles each lasting 24 h, in which 12 h at 40 °C with 80% relative humidity are alternated with 12 h at 30 °C with 60% relative humidity. The environmental variations are automated using a climate chamber, causing continuous precipitation and dissolution from the saline solution. The experiments were carried out at the University of Zaragoza using a saturated solution of Na_2SO_4. Six 3 cm × 3 cm × 3 cm samples of both FGV and CGV were tested. To monitor the evolution of the weathering, half of the samples in each lithotype set were subjected to ten cycles and half to 15 cycles of treatment (Fig. 3). Afterwards, the salts precipitated in the pore network were removed with deionized water prior to porosimetric characterization. The washing procedure was repeated until the samples showed no efflorescence on their surfaces when drying.

3 Results

3.1 Digital Image Analysis for Characterizing Unweathered Rock Structure

3.1.1 Pore Space

3.1.1.1 Macrophotography The resolution range of the acquired macro-photographs is 500 μm–5 cm, which allows an investigation of coarser pore spaces, particularly the wide capillary pores and coarse pores involved in fluid flow transport. The presented data are the averages of the six 25 cm² areas measured for each limestone lithotype (Fig. 4; Table 1). FGV shows rather low porosity at this scale on account of the compact nature of the texture. Conversely, CGV presents high porosity values, especially in the range between 800 μm and 2 mm. The porosimetric distribution curves for the two lithotypes are broadly similar. However, there is a significant difference in pore radius range, with

Fig. 3 Artificial freeze–thaw weathering and salt solution weathering for the two lithotypes. The left-hand panels show photographs of the 5 cm × 5 cm × 5 cm specimens after different numbers of freeze–thaw and saline-solution weathering cycles. The right-hand panels show SEM images of the weathered samples, in which features caused by weathering processes, including secondary products, can be observed
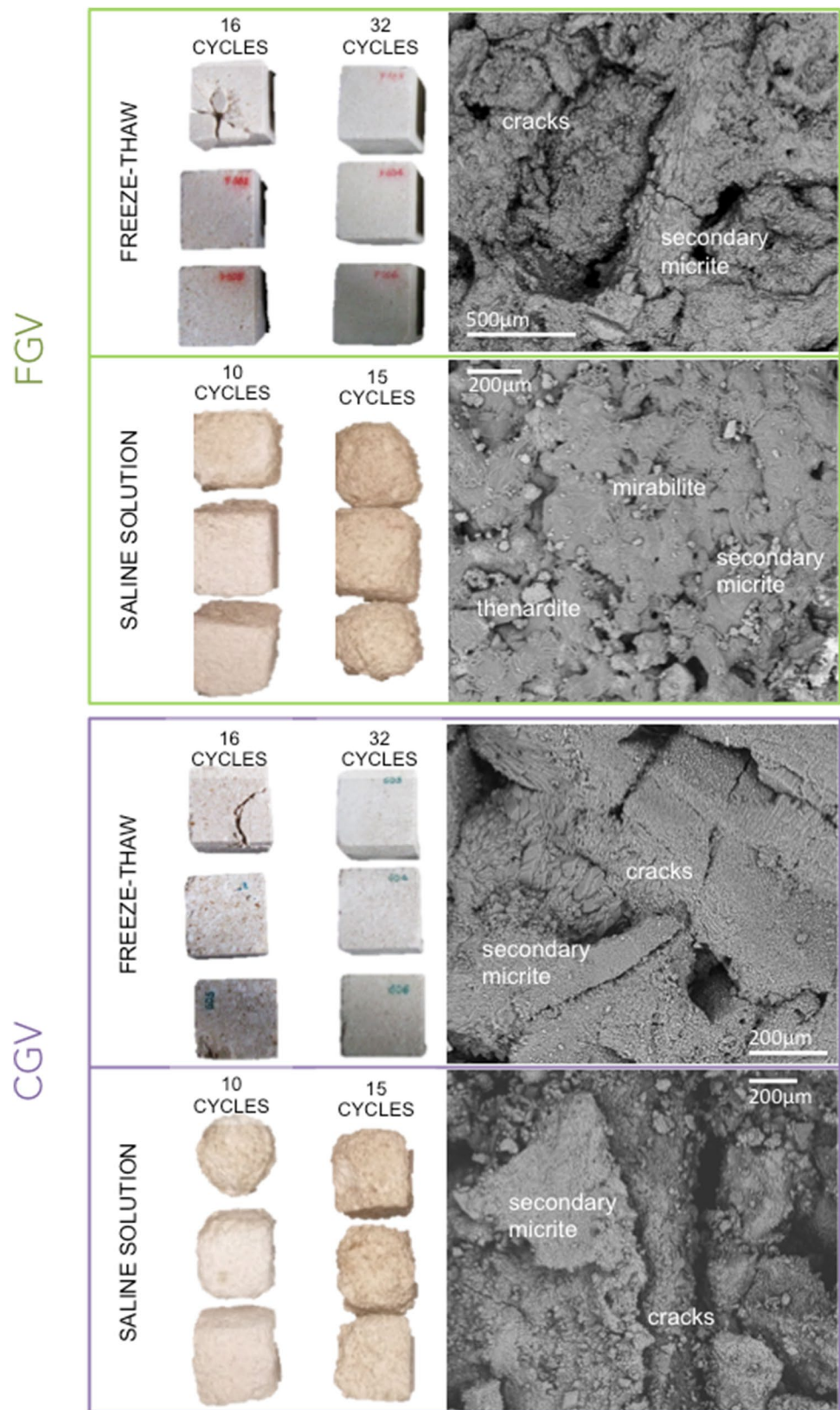
Fig. 4 Porosimetric distribution curves recorded using different techniques (mercury intrusion porosimetry, MIP; digital image analysis, DIA) for unweathered specimens of the different lithotypes (FGV in green and CGV in purple)
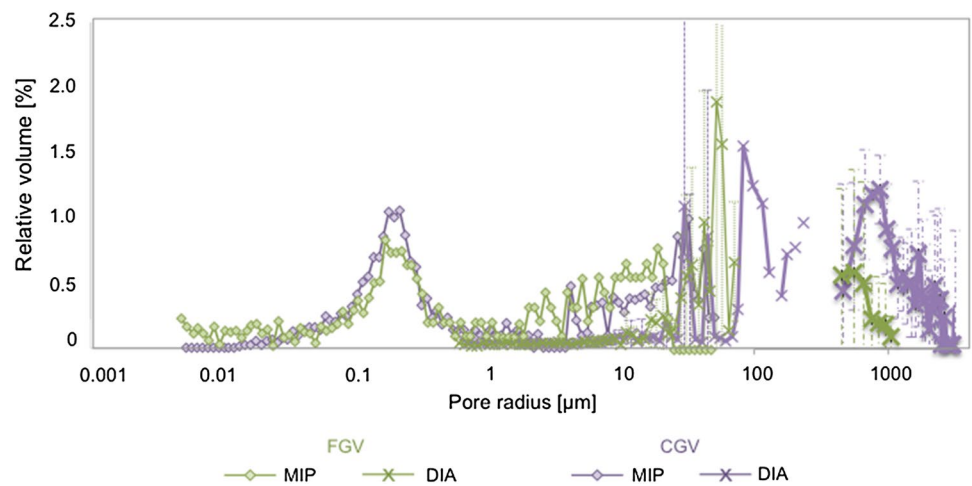

Table 1 Porosimetric values calculated for unweathered specimens using different measurement techniques

ø Range	μm	MIP		DIA (SEM)		DIA (macro)	
		FGV	CGV	FGV	CGV	FGV	CGV
		Relative volume (%)					
Micro	<0.1	5.12	3.25				
Capillary	0.25	5.24	7.25				
	1	4.57	3.88	0.22 ± 0.1	0.27 ± 0.1		
	7.5	5.73	2.84	1.1 ± 0.02	0.89 ± 0.02		
	25	7.17	4.98	1.48 ± 0.1	1.03 ± 0.07		
	75	–	4.55	7.9 ± 0.9	6.06 ± 1.2		
	500				4.55 ± 1.8	0.57 ± 0.4	0.4 ± 0.3
	1000					1.70 ± 0.5	4.94 ± 0.3
Fluid flow	>1000					0.09 ± 0.09	6.3 ± 0.3
Total		27.83	26.77	10.7	12.79	2.36	11.64

Digital image analysis mean values are reported with their corresponding standard deviations

CGV having a wider range (a greater proportion of wider pores), probably as a result of the different sedimentation processes that formed the two lithotypes. The pore space values recorded for the two types are distinct, even considering that the standard deviations are large and reflect the natural variability of the rock. A visual analysis reveals that both lithotypes contain rounded intergranular, fenestral, and vuggy pores.

3.1.1.2 SEM Imaging The resolution range for the SEM-acquired images is c. 1–100 μm, meaning that this technique can be used to investigate only part of the pore space, namely the majority of capillary pores (Fig. 4; Table 1) (micro-porosity results obtained using MPI are discussed in Sect. 3.3).

FGV shows a rather low pore volume of $\Phi = 10.27\%$. The porosimetric distribution curve for FGV shows a peak at 90 μm, with wide fluctuations in relative volume, probably due to pore area refinement during calculations

made using ImageJ. Porosity values in the defined range for CGV are higher than those registered for FGV, with a pore volume of $\Phi = 12.79\%$. The porosimetric distribution curve for CGV presents a peak at 100 μm, with the wide fluctuations in the relative volume values (Fig. 4) probably being due to the dependency of image thresholding on the operator for pore area refinement during calculations with ImageJ. A visual inspection of pore space in the images for the analyzed range (1–100 μm) reveals that both FGV and CGV display elongated pores with high roundness that is mainly interpretable as inter-particle, fenestral, and vuggy porosity.

3.1.2 Grain Orientation

The preferred orientation of grains was examined with respect to the elongation direction of the major bioclasts detectable in macro-photographic images (Fig. 5). In FGV,
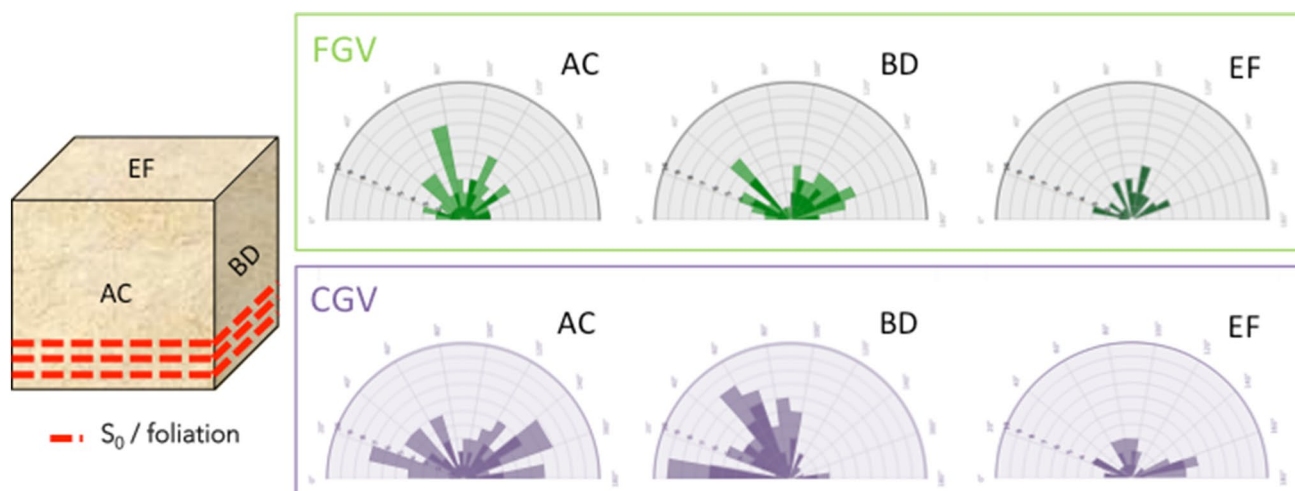
Fig. 5 Image analysis results showing rose diagrams of the orientations of the clasts with respect to the configuration of the cubic specimens for the two lithotypes (FGV and CGV). The darker shading in each case corresponds to the average measured value, and the lighter shading corresponds to the standard deviation of the measurements. No significant preferred orientations are observed

the finer grain size made it difficult to identify such orientation and to measure a large number of clasts. However, for both lithotypes, the distribution of grains orientations does not indicate a preferred orientation of clasts.

3.1.3 Grain Size

The maximum grain size was determined from macrophotographic images. The maximum grain size differentiates the two types, with the maximum grain size in CGV being 2–5 times larger than that in FGV. The high standard deviation of the grain size reflects the natural variability of the samples.

3.2 Relative Mass Loss

Two different weathering trends can be seen in Fig. 6. For salt weathering, the amount of material loss correlates with the time of exposure to the weathering agent. For freeze–thaw cycles, an early decrease in samples mass is followed by a weight increase.

3.3 Mercury Intrusion Porosimetry

The MIP curves for unweathered FGV and CGV samples are characterized by bimodal distributions with a similar trend (Fig. 4). In particular, FGV shows intra-particle spherical porosity (Léon and León 1998) with a bimodal porosimetric distribution (Fig. 7), with the first peak at 0.17 μm and the second at c. 19 μm pore-opening radius. Likewise, CGV presents intra-particle spherical porosity (Léon and León 1998)
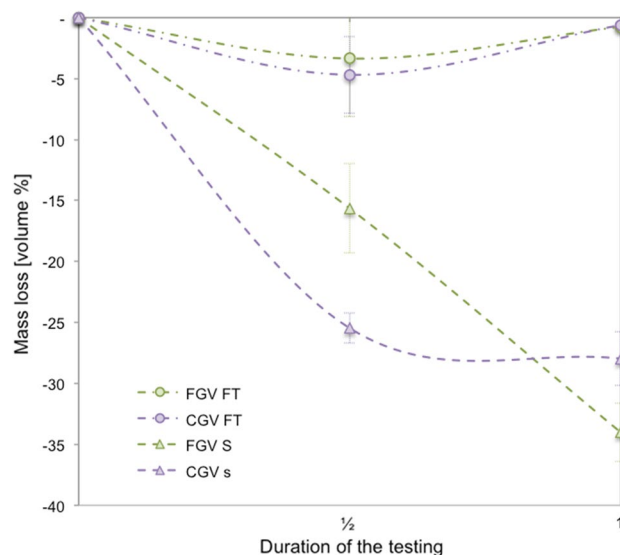

Fig. 6 Relative mass loss of samples during the freeze–thaw (dash–dot lines) and salt-solution (dashed lines) weathering experiments for the two lithotypes (FGV in green and CGV in purple)

with a bimodal porosimetric distribution, with the first peak at 0.19 μm and the second at c. 30 μm pore-opening radius. The comparison between the porosimetric curves obtained for the unweathered samples reveals the presence of wider pores in CGV compared with FGV. The calculated open porosity values for FGV and CGV are similar at 26–27% relative volume (Table 1).

A comparison of the porosimetric curves of unweathered samples with those obtained from the salt-weathered samples allows the effects of the salt-induced weathering processes to be quantified (Fig. 7). For FGV, the open porosity
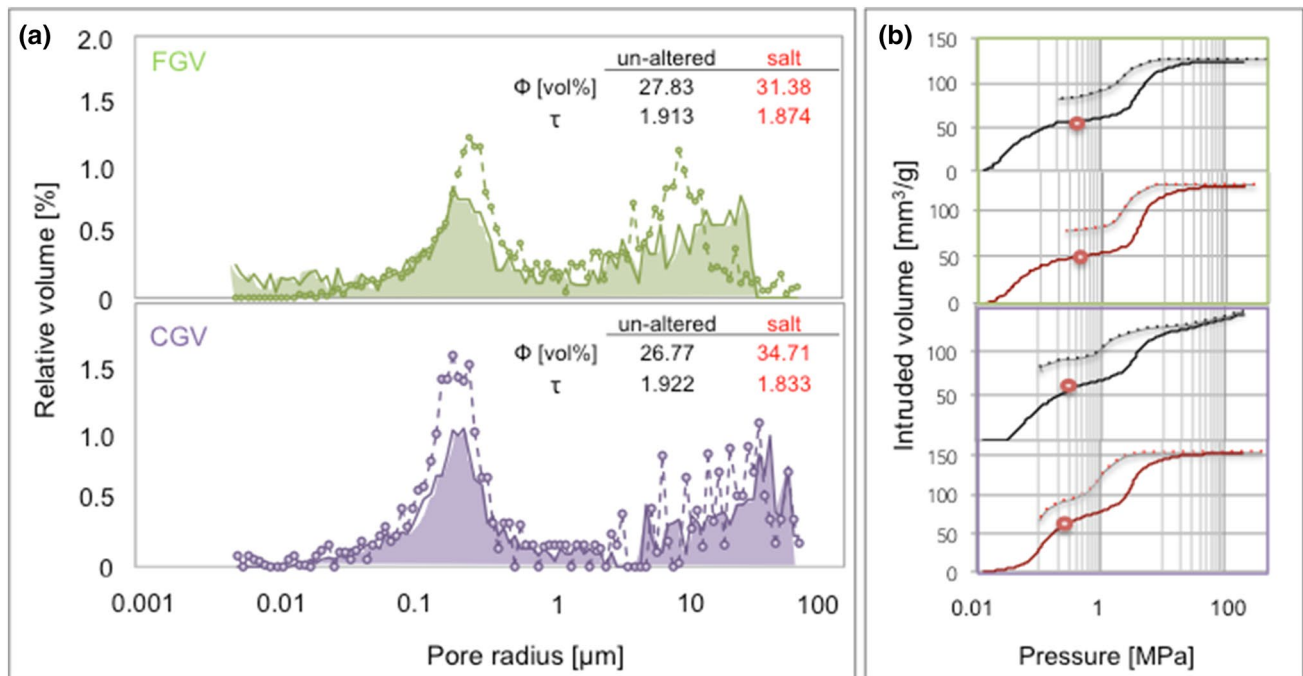
Fig. 7 Mercury intrusion porosimetry test results. **a** Porosimetric distribution curves of FGV and CGV samples before (solid lines and filled areas) and after (dashes) salt weathering. The open poros- ity (Φ) and tortuosity (τ) of unweathered and salt-weathered samples are shown. **b** Pressure/intrusion plot of FGV and CGV samples before (black lines) and after (red lines) salt weathering

value for the salt-weathered sample of $\Phi = 31.38\%$ is higher than that for the unweathered sample ($\Phi = 27.83\%$). In addition, the level of pore interconnection in the weathered sample is higher than that in the unweathered sample, as indicated by the tortuosity values of 1.874 and 1.913, respectively (Fig. 7). The salt-weathered sample shows a bimodal distribution, similar to that of the unweathered sample, but the profile of the porosimetric curve has a different pattern, presenting a higher volume of micro-porosity as well as a higher volume of pores with wider opening radii compared with the unweathered sample (Fig. 7a).

For CGV, the MIP results show a substantial increase in open porosity values from $\Phi = 26.77\%$ to $\Phi = 34.71\%$ after salt-induced weathering. Also, the pore interconnection level of the salt-weathered sample is higher than that of the unweathered sample (tortuosity values of 1.833 and 1.922, respectively). The profiles of the unweathered and salt-weathered sample porosimetric distribution curves are similar, with the main differences being the higher peak for the salt-weathered curve at c. 0.18 μm and the more variable values between 8 and 90 μm, indicating higher open porosity levels (Fig. 7a).

After salt-induced weathering, the relationship between intruded volume and pressure shows a slight increase in intra-particle porosity after salt weathering (Fig. 7b).

The porosimetric distribution curves of the unweathered samples allowed to recast Maage Durability Factor and Salt Susceptibility Index for both lithotypes. Values of the Maage Durability Factor indicate that both lithotypes are prone to freeze–thaw weathering ($F_c = 31$ for FGV and $F_c = 36$ for CGV). In addition, the calculated SSI values indicate that both lithotypes are susceptible to salt weathering (SSI = 7.51 for FGV and SSI = 6.62 for CGV).

3.4 Total Immersion

Both of the Vicenza Stone lithotypes showed a marked increase in absorbed water volume during the immersion tests, indicating the presence of highly interconnected open pores (Fig. 8). For both FGV and CGV, the absorption curves (Fig. 8a, left-hand panel) show different behaviors for freeze–thaw-weathered and salt-weathered samples. The curve rise for the freeze–thaw-weathered samples is less steep than that for the unweathered samples, reflecting lower suction pressures and lower water absorption rates. In contrast, the curve rise for the salt-weathered samples is steeper than that of the unweathered samples, reflecting a higher rate of water absorption.

Evaporation curves (Fig. 8a, right-hand panel) were constructed for unweathered and salt-weathered samples to evaluate the influence of weathering during drying. The
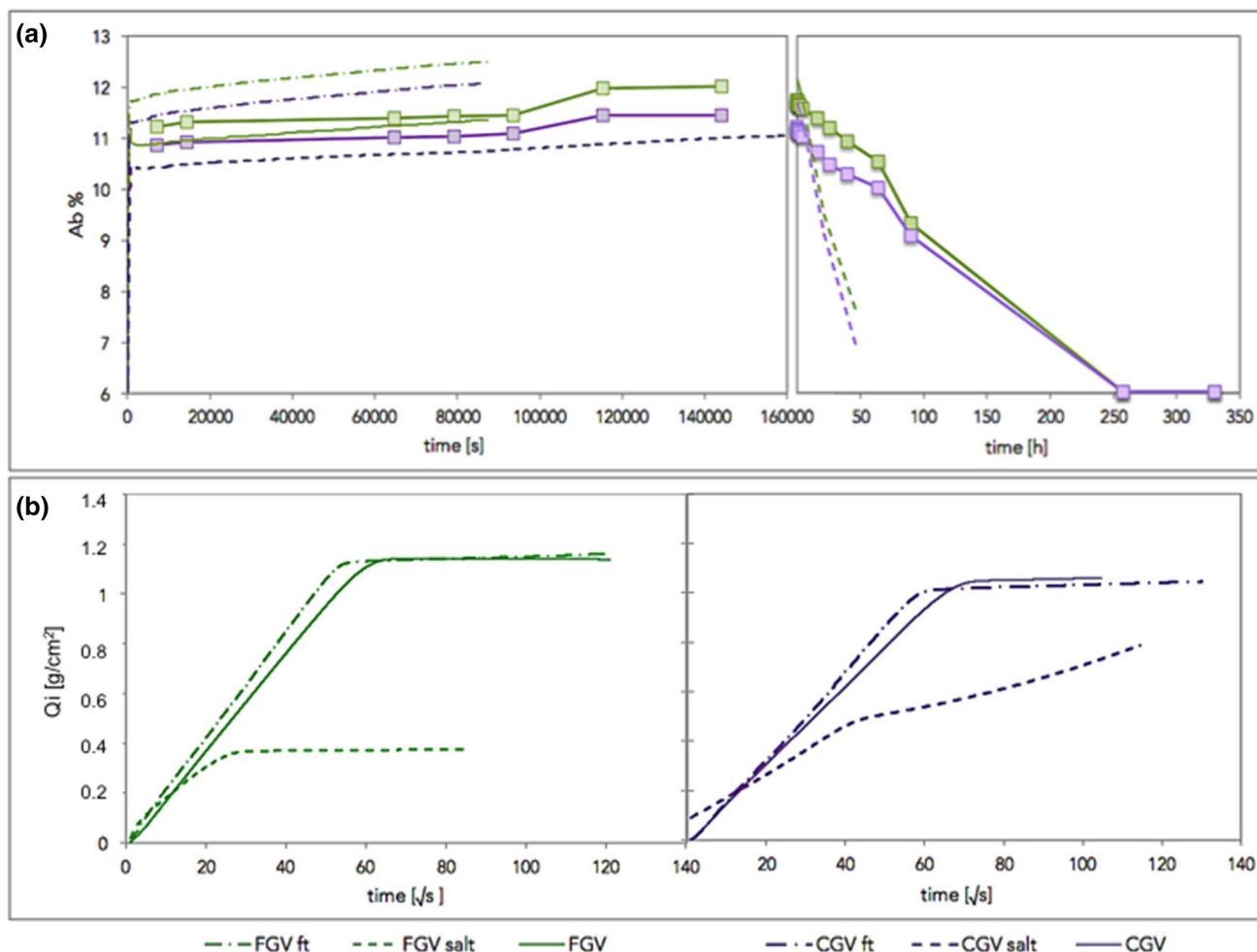
Fig. 8 Hydraulic test results for unweathered (solid lines), freeze–thaw (*ft* dash–dot lines), and salt-weathered (salt; dashes) samples of FGV (in green) and CGV (in purple). **a** Water absorption for total immersion and evaporation experiments. **b** Absorbed water per unit area for capillary rise experiments

fresh samples present a gradual decrease in the amount of water trapped within the pore network and eventually attain almost complete evaporation, whereas the salt-weathered samples present a more rapid decrease in water content. The increase of air circulation due to the modification to the porous network induced by salt weathering allows a faster drying process and, therefore, the testing procedure registers highest evaporation rates.

3.5 Capillary Uptake

Water absorption curves recorded for FGV and CGV show a similar trend, characterized by a linear increase followed by a flattening when the system reaches equilibrium between capillary uptake and evaporation (Fig. 8b). A comparison of the data obtained from unweathered and salt-weathered samples reveals that both FGV and CGV show advanced

levels of weathering, especially from dissolution and recrystallization, accompanied by an overall enlargement of the pre-existing pore throats, corresponding to lower values of the capillary water absorption coefficient. Conversely, a comparison of the data obtained from unweathered and freeze–thaw-weathered samples reveals a higher rate of water uptake in the latter, suggesting the formation of micro-cracks.

3.6 Ultrasound Velocity

Unweathered specimens of both lithotypes show similar fast and slow ultrasound velocities, resulting in low anisotropy coefficients (Fig. 9; Table 2). The lower ultrasound velocities after salt weathering suggest a higher void volume (as air is insulating). Moreover, the anisotropy coefficient values suggest that the alteration of the porous network during salt weathering developed along a preferred orientation

Fig. 9 Ultrasound velocity test results showing a comparison between fast (perpendicular to bedding; in green) and slow (parallel to bedding; in orange) propagation directions, and between unweathered (solid lines and filled areas) and artificially weathered samples (dashed lines = salt weathering; dash–dot lines = freeze–thaw)
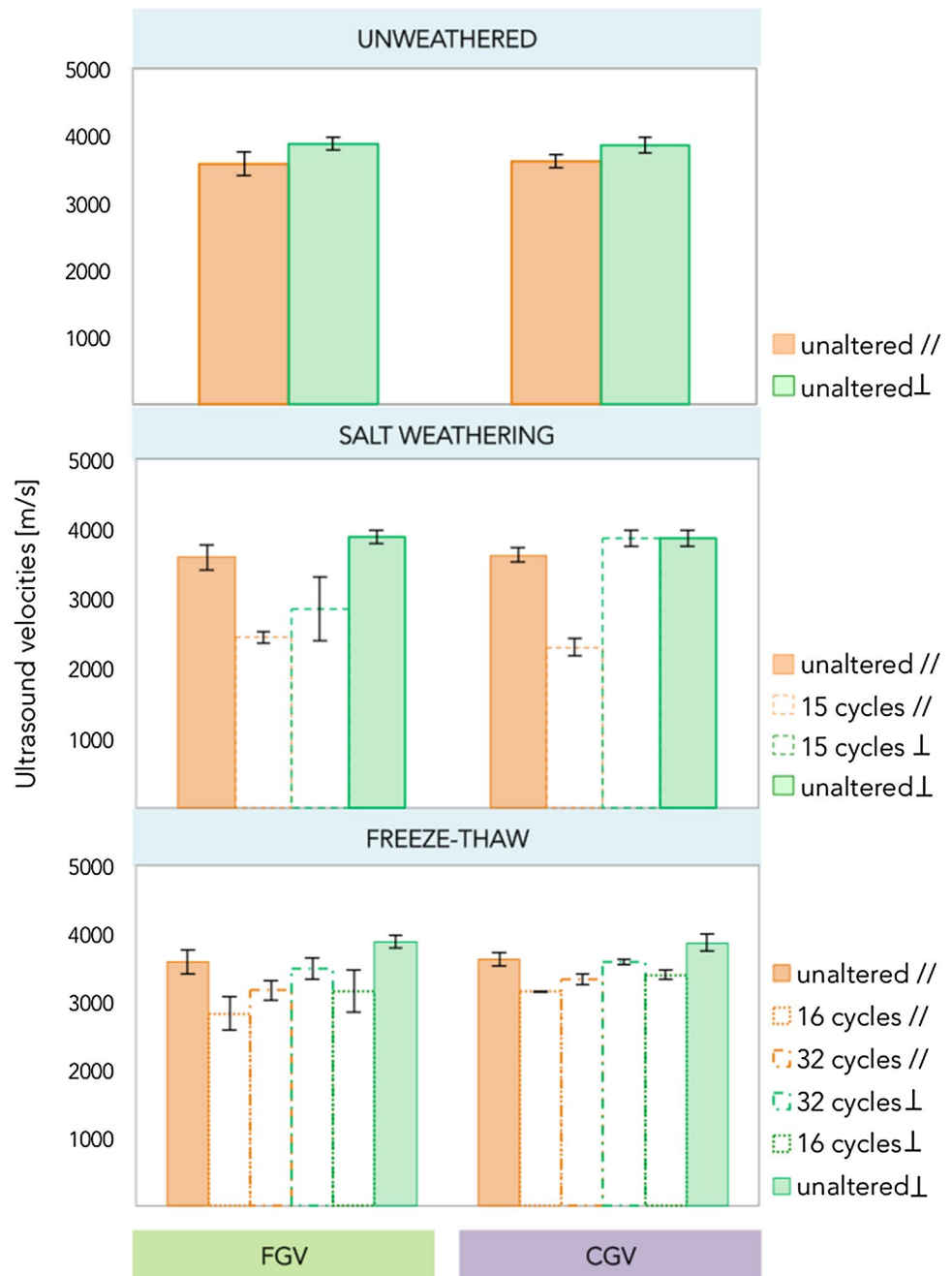

Table 2 Ultrasound measurement results: anisotropy coefficients

	FGV		CGV	
	Average	St.deviation	Average	St.deviation
Unweathered	6.5	1.5	7.5	3.5
Freeze–thaw weathered	7.6	2.2	10.8	1.2
Salt weathered	21.3	15.7	13.3	0.2

(Table 2). In particular, the analysis of the attenuation of the ultrasound velocity suggests that voids are generated perpendicular to the sedimentation layers. Further, the attenuation of ultrasound velocities is higher after 16 cycles and lower after 32 cycles of freeze–thaw experimental weathering. The evolution of ultrasound velocities in the samples affected by freeze–thaw weathering suggests hardening after early, severe weathering (Martínez-Martínez et al. 2013).

4 Discussion

The multiple-technique approach adopted in the present study allowed the textural properties of the two studied limestone lithotypes to be well characterized using instruments with different resolution ranges. Macrophotograph-based image analysis resolved both maximum grain size and pore space for $r > 400$ µm, SEM-based DIA resolved pore space within $1 < r < 200$ µm, and MIP resolved pore space within $0.01 < r < 75$ µm. The combination of petrographic and petrophysical data analyses enables a better understanding to be gained of the mechanisms (chemical and mechanical) involved in weathering. In the case of FGV, the combined data suggest that salt weathering induces both a mechanical effect (i.e., enlargement of the small pores or throats of 0.2 µm radius) and chemical effects from dissolution (i.e., a widening of the radii of pores measuring c. 100 µm) and from secondary precipitation inside the larger pores (i.e., a reduction in the opening radius of pores measuring c. 9 µm for the widest voids), with an increase in the degree of pore interconnection and in overall porosity. The modification of pore radii recorded by MIP agrees well with the hydraulic test curve variations and SEM images, suggesting a coherence and reliability of the results.

The total immersion and capillary rise tests revealed the widening of the major openings of the pore network that occurred during salt weathering, which resulted in lower suction pressures and lower absorption rates, associated with a lengthening of the time span over which the samples reached complete water absorption. SEM images (Fig. 3) verify the precipitation of secondary fine-grained calcite on surfaces and inside the pores, implying the occurrence of chemical weathering.

The evolution of samples during the freeze–thaw-weathering experiments was investigated using mass loss measurements, hydraulic tests, and ultrasound. The resulting data revealed a marked decrease in cohesion with material loss during a first phase of major damage to the host material. This was followed by the reprecipitation of calcite from the saturated water inside the pore network, which led to a subsequent material hardening phase and overall mass increase. These processes generate the formation of micro-cracks, resulting in the more rapid absorption of water and a greater volume of water. The process of freeze–thaw causes the formation of micro-cracks opening in all directions (as indicated by the lack of significant variation in the anisotropy coefficient). Compared with the fresh Vicenza Stone specimens, the weathered samples in the total immersion and capillary rise tests show a higher rate of water absorbance, which is likely attributable to the development of micro-cracks. These micro-cracks form as a response to mechanical stress, in addition to the secondary chemical processes of dissolution–precipitation occurring on the material surface, as verified by SEM imaging.

In the case of CGV, the combined data suggest that salt weathering induces both a mechanical effect (i.e., the formation of micro-cracks measuring 0.1 µm) and chemical effects by dissolution (i.e., a widening of pores measuring c. 0.2 µm) followed by precipitation inside the larger pores (i.e., shrinkage of pores measuring 9–100 µm), with an overall increase in open porosity. The profiles of the unweathered and salt-weathered porosimetric distribution curves are very similar, with the main differences being the higher peak for the salt-weathered curve at c. 0.18 µm and the more variable values c. 8–90 µm, indicating higher open porosity levels and the formation of micro-cracks perpendicular to the sedimentation layers, also visible in SEM images (Fig. 3). The hydraulic test results indicate that saline solutions also induce chemical weathering processes in addition to mechanical processes, widening the pore network and resulting in a less steep curve rise, lower suction pressures, and lower absorption rates in the weathered material compared with the fresh material. The enlargement of the pre-existing throats due to the action of salt weathering generates a dilatation of the time span, in which the samples are fully absorbed in water, therefore, after the same time interval the total volume accessible to water (V_w) appears to be smaller in the salt-weathered samples. Mass loss data, ultrasound and hydraulic tests on freeze–thaw aged samples highlighted a secondary hardening phase with the deposition inside the pore network of calcite from the saturated solution, after a first major damage phase. The involved processes generate the formation of micro-cracks, resulting in a faster increase of volume of absorbed water.

In summary, FGV shows a high weathering rate for both types of artificial weathering experiment (freeze–thaw and salt weathering), as predicted by the durability factors calculated using the MIP data. After the experimental freeze–thaw-weathering cycles, micro-cracks formed, and after weathering in saline solution, mechanically and chemically induced stresses developed, leading to a marked increase in open porosity (MIP showed an increase from 27% up to 31% in open pore volume during the salt-weathering experiments). The simultaneous occurrence of dissolution and precipitation processes suggests the concurrent action of chemical and mechanical processes. CGV showed signs of physical stress after freeze–thaw weathering and pervasive chemical degradation due to salt weathering. The stresses induced by salt weathering produced a significant increase in open porosity (MIP registered an increase from 26 to 34% in volume during the salt-weathering experiments). FGV underwent more severe weathering compared with CGV, especially when exposed to saline solution, possibly because of the presence of a

larger reactive surface (compared with CGV, and increasing with secondary precipitation) and a pore radius distribution prone to mechanical stress induced by the precipitation and growth of Na_2SO_4 crystals (Flatt et al. 2017). The comparison of all the acquired data shows that FGV has lower durability than the CGV lithotype when exposed to outdoor conditions characterized by salt-based weathering.

5 Conclusion

This multiple-technique study investigated the difference in durability of two ornamental limestone (Vicenza Stone) lithotypes by measuring the textures and porosity pertinent to salt- and freeze–thaw-weathering processes. Both grain size and porosity were shown to have a significant influence on the intensity of weathering processes and on the development of weathering. The results indicate that this limestone is susceptible to weathering agents when exposed to outdoor environments. However, the two lithotypes showed different weathering susceptibilities, with the fine-grained lithotype proving to be particularly prone to salt weathering, whereas the coarse-grained lithotype is susceptible to the wide thermal excursions of freeze–thaw weathering.

References

Ballesteros EM, Talegón JG, Iñigo ACI et al (2011) Importance of porosity and transfer of matter in the rock weathering processes: Two examples in central Spain. Environ Earth Sci 64:1741–1754. https://doi.org/10.1007/s12665-011-1015-y

Benavente D (2011) Why pore size is important in the deterioration of porous stones used in the built heritage. Macla 15:41–42. https://doi.org/10.1007/s12665-010-0815-9.transported

Benavente D, García Del Cura MA, Bernabéu A, Ordóñez S (2001) Quantification of salt weathering in porous stones using an experimental continuous partial immersion method. Eng Geol 59:313–325. https://doi.org/10.1016/S0013-7952(01)00020-5

Bosellini FR, Trevisani E (1992) Coral facies and cyclicity in the Castelgomberto Limestone (Early Oligocene, Easterr Lessini Mountains, Northern Italy). Riv Ital Paleont Strat 98(3):339–352

Cornale P, Rosanò P (1994) Le pietre tenere del Vicentino. Uso e restauro. La Grafica & Stampa Ed. s.r.l., Vicenza

Crawford EC, Mortensen JK (2009) An ImageJ plugin for the rapid morphological characterization of separated particles and an initial application to placer gold analysis. Comput Geosci 35:347–359

Di Benedetto C, Cappelletti P, Favaro M et al (2015) Porosity as key factor in the durability of two historical building stones: Neapolitan Yellow Tuff and Vicenza Stone. Eng Geol 193:310–319. https://doi.org/10.1016/j.enggeo.2015.05.006

Dunham RJ (1962) Classification of Carbnate Rocks according to depositional texture. In: Ham WE (ed) Classification of carbonate rocks. AAPG, Tulsa, pp 108–121

Flatt R, Aly Mohamed N, Caruso F et al (2017) Predicting salt damage in practice: a theoretical insight into laboratory tests. RILEM Tech Lett 2:108. https://doi.org/10.21809/rilemtechlett.2017.41

Folk RL (1959) Practical petrographic classification of limestones. Am Assoc Pet Geol Bull 43:1–38

Folk RL (1962) Spectral subdivision of limestone types. In: Classification of carbonate rocks—a symposium: American Association of Petroleum Geologists Memoir, vol 1, pp 62–84

Franzoni E, Sassoni E (2011) Correlation between microstructural characteristics and weight loss of natural stones exposed to simulated acid rain. Sci Total Environ 412–413:278–285. https://doi.org/10.1016/j.scitotenv.2011.09.080

Gioncada A, Leoni L, Lezzerini M, Miriello D (2011) Relationships between mineralogical and textural factors in respect to hydric dilatation of some sandstones and meta-sandstones from the Northern Apennine. Ital J Geosci 130:394–403. https://doi.org/10.3301/IJG.2011.16

Iñigo AC, Vicente MA, Rives V (2000) Weathering and decay of granitic rocks: Its relation to their pore network. Mech Mater 32:555–560. https://doi.org/10.1016/S0167-6636(00)00027-2

Kahraman S (2007) The correlation between the saturated and dry P-wave velocity of rocks. Ultrasonics 46:341–348

Léon Y, León CA (1998) New perspectives in mercury porosimetry. Adv Colloid Interface Sci 76–77:341–372. https://doi.org/10.1016/S0001-8686(98)00052-9

Martínez-Martínez J, Benavente D, Gomez-Heras M et al (2013) Nonlinear decay of building stones during freeze-thaw weathering processes. Constr Build Mater 38:443–454. https://doi.org/10.1016/j.conbuildmat.2012.07.059

Mattioli M, Cenni M, Passaglia E (2016) Secondary mineral assemblages as indicators of multistage alteration processes in basaltic lava flows: evidence from the Lessini Mountains, Veneto Volcanic Province, Northern Italy. Period di Miner 85:1–24. https://doi.org/10.2451/2015PM0375

Molina E, Cultrone G, Sebastián E et al (2011) The pore system of sedimentary rocks as a key factor in the durability of building materials. Eng Geol 118:110–121. https://doi.org/10.1016/j.enggeo.2011.01.008

Mueller U, Hansen EF (2001) Use of digital image analysis in conservation of building materials. In: Georgali B, Toumbakari EE (eds) Proceedings of the 8th Euroseminar on microscopy applied to building materials. Cosmosware, Athens, pp 603–610

Plattner SH, Reale R, Visco G et al (2012) Proposal of a new analytical procedure for the measurement of water absorption by stone. Preliminary study for an alternative to the Italian technical normative NORMAL 07-81. Chem Cent J 6:1. https://doi.org/10.1186/1752-153X-6-62

Roduit N (2007) JMicroVision: un logiciel d'analyse d'images pétrographiques polyvalent. Faculty of Sciences, University of Genève, Doctoral Thesis, No. 3830

UNI 11186:2008 (2008) Cultural heritage—Natural and artificial stone—Methodology for exposure to freeze-thawing cycles

UNI EN 13755:2008 (2008) Natural stone test methods—Determination of water absorption at atmospheric pressure

UNI EN 15801:2010 (2010) Conservation Of Cultural Property—Test Methods—Determination of water absorption by capillarity

Yu S, Oguchi CT (2010) Role of pore size distribution in salt uptake, damage, and predicting salt susceptibility of eight types of Japanese building stones. Eng Geol 115:226–236. https://doi.org/10.1016/j.enggeo.2009.05.007